HAL
open science

Hydration of Na-saturated Synthetic Stevensite, a Peculiar Trioctahedral Smectite

Doriana Vinci, Martine Lanson, Valérie Magnin, Nathaniel Findling, Bruno Lanson

To cite this version:

Doriana Vinci, Martine Lanson, Valérie Magnin, Nathaniel Findling, Bruno Lanson. Hydration of Na-saturated Synthetic Stevensite, a Peculiar Trioctahedral Smectite. Clay Minerals, 2020, 10.1180/clm.2020.32 . insu-03022632

HAL Id: insu-03022632

https://insu.hal.science/insu-03022632

Submitted on 25 Nov 2020

HAL is a multi-disciplinary open access archive for the deposit and dissemination of scientific research documents, whether they are published or not. The documents may come from teaching and research institutions in France or abroad, or from public or private research centers.

L'archive ouverte pluridisciplinaire **HAL**, est destinée au dépôt et à la diffusion de documents scientifiques de niveau recherche, publiés ou non, émanant des établissements d'enseignement et de recherche français ou étrangers, des laboratoires publics ou privés.

Hydration of Na-saturated Synthetic Stevensite, a Peculiar Trioctahedral Smectite

Doriana Vinci[1,2], Bruno Lanson[1,*], Martine Lanson[1], Valérie Magnin[1], Nathaniel Findling[1]

Univ. Grenoble Alpes, Univ. Savoie Mont Blanc, CNRS, IRD, Univ. Gustave Eiffel, ISTerre, F-38000 Grenoble, France

Dipartimento Scienze Terra & Geoambientali, Univ. Bari Aldo Moro, Bari, Italy

Running title: Hydration of Na-saturated Synthetic Stevensite

*. Corresponding author: bruno.lanson@univ-grenoble-alpes.fr

Abstract

Smectite interlayer water plays a key role on the mobility of elements and molecules, but also in a variety of geological processes. In contrast to saponite and hectorite, whose layer charge originates from isomorphic substitutions, stevensite layer charge originates from the presence of octahedral vacancies. Despite its common occurrence in lacustrine environments, hectorite hydration has received little attention, compared to saponite and hectorite. Early reports mention a specific hydration behavior, however, with the systematic presence of a low-angle reflection attributed to the regular interstratification of different hydration states. The present study aims at revisiting this specific hydration behavior in more depth. Within this scope, the hydration behavior of the above three smectite varieties are compared using synthetic trioctahedral smectites of similar layer charge, and different compositions of their octahedral sheets. The chemical composition of the octahedral sheet does not appear to influence significantly smectite hydration for saponite and hectorite. Compared to its saponite and hectorite equivalents, H_2O content in stevensite is lower by ~2.0 mmol H_2O per g of dry clay. Consistent with this lower H_2O content, Zn-stevensite lacks a stable monohydrated state, dehydrated layers prevailing from 60 to 0% RH. The presence of the regular interstratification of 0W and 1W layers is responsible for the low-angle reflection commonly observed for stevensite under air-dried conditions. Finally, stevensite identification method based on X-ray diffraction of heated and EG-solvated samples is challenged by the strong influence of octahedral sheet chemical composition (Zn or Mg in the present study) on hectorite swelling behavior. The origin of this effect remains undetermined and further work is needed to propose a more general identification method.

Keywords: Smectite hydration, stevensite, smectite identification

Introduction

Smectites are phyllosilicates whose 2:1 layers consist of two tetrahedral sheets sandwiching an octahedral one. In trioctahedral smectites the three octahedral sites are all occupied by divalent cations, usually Mg^{2+}. Isomorphic substitutions occurring either in tetrahedral or in octahedral sheets (Al-for-Si and Li-for-Mg, respectively) or the presence of vacant octahedral sites induce a layer charge deficit which is compensated for by the presence of hydrated exchangeable cations within smectite interlayers and at the mineral surface. Based on the origin of the layer charge deficit, trioctahedral smectites have received different mineral names: saponite, hectorite, and stevensite for tetrahedral substitutions, octahedral substitutions and octahedral vacancies, respectively (Brindley, 1980). Following the pioneering works of Nagelschmidt (1936) and Bradley *et al*. (1937), smectite hydration has drawn a lot of attention, owing to the key influence played by smectite interlayer water on the mobility of contaminants and nutrients (Laird *et al.*, 1991), but also in a variety of geological settings (See Ferrage *et al.*, 2010, and references therein). The influence of the amount and location of isomorphic substitutions on trioctahedral smectite (saponite and hectorite) hydration has been extensively investigated over the last decade or so (Ferrage *et al.*, 2005a, 2010, 2011; Malikova *et al.*, 2005, 2007; Michot *et al.*, 2005, 2007, 2012; Rinnert *et al.*, 2005; Dazas *et al.*, 2015; Vinci *et al.*, 2020). This interest has been sustained by the frequent use of smectite in natural and engineered barriers in (nuclear) waste repositories and by the related requirements for their safety assessment. In both saponite and hectorite, the presence of discrete hydration states similar to those reported in the pioneering works on smectite hydration (Bradley *et al.*, 1937; Mooney *et al.*, 1952; Norrish, 1954b) leads to the well-known stepwise expansion of the layer-to-layer distance. With increasing water activity, the occurrence of dehydrated layers (0W, d_{001} = 9.6–10.2 Å) is followed by 1W, 2W, and 3W hydration states (d_{001} = 11.6–12.9 Å, d_{001} = 14.9–15.7 Å, d_{001} = 18–19 Å, respectively), corresponding to the intercalation of 1, 2, and, less frequently, 3 “planes” of interlayer H_2O molecules.

Stevensite, whose layer charge deficit originates from the presence of octahedral vacancies, is a common smectite in lacustrine environments (Eberl *et al.*, 1982; Khoury *et al.*, 1982; Jones, 1986; Thiry *et al.*, 2014; Bentz and Peterson, 2020; De Oliveira Nardi Leite *et al.*, 2020) By contrast, hydration of stevensite, whose layer charge deficit originates from the

presence of octahedral vacancies. Compared to saponite and hectorite, its hydration has received much less attention although early reports mention a very specific behavior (Brindley, 1955; Faust *et al.*, 1959; Shimoda, 1971). In particular, these studies systematically mention the occurrence of a low-angle reflection tentatively assigned to the regular alternation of 0W and 2W layers (Brindley, 1955). The present study thus aims at revisiting this peculiar hydration behavior in more depth. For this purpose, two stevensite samples, with Zn- and Mg-rich octahedral sheets, were hydrothermally synthesized together with their saponite and hectorite chemical equivalents. All synthesized samples have similar layer charge deficits of ~0.8 e^- per $O_{20}(OH)_4$. Hydration of all samples was systematically assessed using volumetric H_2O vapor (de)sorption isotherms and X-ray diffraction under controlled humidity conditions. Quantitative profile fitting of X-ray diffraction data was used both to assess the relative proportions of the different hydrates and the evolution of these proportions as a function of H_2O activity, and to unravel the origin of the low-angle reflection, if any.

Materials and methods

Sample preparation

Three varieties of Zn-rich trioctahedral smectites and one Mg-stevensite were synthesized hydrothermally from gel precursors having adequate stoichiometry (Hamilton & Henderson, 1968). Preparation of a sauconite with ideal structural formula $[Na_{0.8}]^{inter}[Zn_{6.0}]^{octa}[Si_{7.2}Al_{0.8}]^{tetra}O_{20}(OH)_4$ (hereafter referred to as Zn-sap), a Zn equivalent of hectorite with ideal composition $[Na_{0.8}]^{inter}[Zn_{5.2}\ Li_{0.8}]^{octa}[Si_{8.0}]^{tetra}O_{20}(OH)_4$ (hereafter referred to as Zn-hect); a Zn equivalent of stevensite with ideal structural formula $[Na_{0.8}]^{inter}[Zn_{5.6}\square_{0.4}]^{octa}[Si_{8.0}]^{tetra}O_{20}(OH)_4$ (hereafter referred to as Zn-stev), and stevensite with an ideal structural formula $[Na_{0.8}]^{inter}[Mg_{5.6}\square_{0.4}]^{octa}[Si_{8.0}]^{tetra}O_{20}(OH)_4$ (hereafter referred to as Mg-Stev) was sought. All structural formulae are derived from the stoichiometry of gel precursors. Such an ideal sauconite composition leads however to the crystallization of a hemimorphite impurity ($Zn_4Si_2O_7(OH)_4{\cdot}H_2O$) and a lower Zn content is necessary to obtain pure sauconite (Higashi *et al.*, 2002). The Na:Al:Si:Zn ratio of the initial gel was thus modified to 0.8:0.8:7.2:5.0 leading to the following approximate structural formula: $[Na_{0.84}]^{inter}[Zn_{5.24}Al_{0.38}\square_{0.38}]^{octa}[Si_{7.53}Al_{0.47}]^{tetra}O_{20}(OH)_4$. Synthesis of Zn-smectites was

performed in Teflon lined Parr reactor (45mL). Initial gels were treated hydrothermally under autogenous pressure for 2 weeks at 170 °C for Zn-stev and Zn-hect, and for 3 days at 220 °C for Zn-sap. Mg-stev synthesis was performed in an externally heated Morey-type pressure vessel with an internal silver tubing (Robert *et al.*, 1993; Bergaoui *et al.*, 1995). Synthesis conditions were a temperature of 300 °C, a water pressure of 500 bars, and a duration of 2 weeks. After synthesis, all samples were Na-saturated by contact with a 1 mol L^{-1} aqueous solution of NaCl. To ensure a complete exchange of interlayer cations, samples were shaken mechanically in this NaCl solution for 24 h before separation of the solid fraction by centrifugation. Excess NaCl was then removed by washing the solid three times with deionized water (Siemens UltraClear, 18.2 MΩ cm^{-1}) and separation of the solid fraction by centrifugation.

Experimental Sample Characterization

Water vapor sorption isotherms were determined volumetrically at 25 °C from sample powder using a Belsorp-max instrument from BEL Japan. Lyophilized aliquots (∼100 mg) were initially outgassed at 150 °C for 24 h under a residual pressure of 10^{-5}–10^{-4} Pa. In addition, N_2 BET surface areas were determined on all Na-saturated samples with the same instrument.

Oriented slides were prepared for all samples by pipetting an aqueous clay slurry on glass slides and drying it at room temperature. The amount of deposited material was weighed. An aluminum slide was used for sauconite preparation to overcome peeling and curling issues. X-ray diffraction (XRD) patterns were then recorded using a Bruker D8 diffractometer operated at 40 kV and 40 mA and equipped with a MHG Messtechnik humidity controller coupled to an Anton Paar CHC+ chamber. Intensities were measured for 6s per 0.04 °2θ step over the 2−50 °2θ Cu Kα angular range with a SolXE Si(Li) solid-state detector (Baltic Scientific Instruments). Divergence slit, the two Soller, antiscatter, and resolution slits were 0.3°, 2.3°, 0.3°, and 0.1°, respectively. Samples were maintained at 23 °C in the CHC+ chamber during data collection, whereas the desired relative humidity (RH) value was maintained by using a constant flow of mixed dry/saturated air. RH was continuously monitored with a hygrometer (uncertainty of ∼2% RH) located close to the sample along the whole isotherm. Samples were equilibrated at ∼95% RH for 8h (Mg-stev) or 4h (Zn-hect, Zn-sap, and Zn-stev) before starting data collection. Along the desorption isotherm, samples were equilibrated for 2 h at each given RH value before XRD data collection, hydration stability being systematically checked by

129 recording again the low-angle reflection after collection of a complete XRD pattern. In
130 addition, all samples were exposed to ethylene glycol (EG) vapor (40 °C) overnight before XRD
131 data collection at 23 °C and room temperature. XRD data was also collected after a similar EG
132 solvation of samples heated to 350 °C for 1 h. Routine data processing, including
133 determination of basal reflection FWHM, was performed using the Eva® program from Bruker.
134 XRD data modeling was performed as described previously (Ferrage *et al.*, 2005a, 2005b, 2010;
135 Dazas *et al.*, 2015; Vinci *et al.*, 2020). Briefly, a main structure, periodic (that is with only one
136 layer type) if possible, was used to reproduce as much as possible of the data. Additional
137 contributions to the diffracted intensity were then introduced to account for the misfit. Up to
138 four interstratified structures, each with a different composition (relative proportion of the
139 different layer types), were necessary to reproduce some of the XRD patterns because of the
140 observed hydration heterogeneity. Interstratification of the different types of hydrated layers
141 was essentially random in all contributions to the diffracted intensity. Ordered
142 interstratification was used to reproduce low-angle reflections, however. In this case, the
143 Reichweite parameter was set to 1, and maximum possible degree of ordering was
144 considered, thus prohibiting the succession of two layers of the minor layer type (Drits &
145 Tchoubar, 1990; Sakharov & Lanson, 2013).

146

147 **Results and discussion**

148 *Powder X-ray diffraction*

149 Hydration modification of Zn-rich stevensite along the desorption isotherm induces a steady
150 decrease of the *d*-spacing corresponding to the first basal reflection from ~15.9 Å to ~10.1 Å
151 at 90% and 10% RH, respectively (Figs. 1A, SI1). Except for the peak at 3.1-3.2 Å, which is
152 common to all usual hydration states (0W, 1W, 2W, and 3W), higher-order reflections are
153 weak and do not define a rational series of 00*l* reflections (Fig. 1A), indicative of a major
154 hydration heterogeneity. By contrast, a low-angle reflection, that is likely related to the
155 regular alternation of two hydration states, is visible at 21-22 Å for XRD patterns collected
156 from 70 to 30% RH (arrows in Fig. 1A). Upon EG solvation, Zn-stev d_{001} increases to ~17.1 Å, as
157 expected for smectite (Fig. 1B), and positions of 002 and 005 reflections are about rational
158 with that of the 001, thus indicating little interstratification with non-swelling layers, if any. In

addition, the presence of a significant amount of talc-like layers Zn-stev would, after EG solvation, induce a significant broadening of the first basal reflection compared to reflections occurring at higher angle, inconsistent with the data (Fig. SI2). Hydration behavior of Zn-sap and Zn-hect (Figs. SI3, SI4) are consistent with those of their Mg equivalent having similar layer charge (Fig. 1 in Ferrage *et al.*, 2010; Fig. 2 in Dazas *et al.*, 2013) and indicate slightly higher hydration at low RH values. Position of smectite first basal reflection at 20% RH correspond indeed to an apparent layer-to-layer distance of 10.2 Å for Zn-stev compared to 12.4 and 11.6 Å for Zn-sap and Zn-hect, respectively (Fig. 1B – 12.35 and 12.45 Å for Mg-sap and Mg-hect, respectively).

XRD patterns of Mg-stev collected along the water vapor desorption isotherm differ significantly from those of its Zn counterpart (Fig. 2A). Specifically, the first basal reflection is systematically located between the positions expected for 1W and 0W smectite, thus indicating a consistently low hydration state, possibly as the result of an incomplete rehydration after drying. Rehydration of stevensite (both Zn- and Mg-stev) appears indeed to be slow (up to several days or even weeks) after drying the sample. The position of this first basal reflection steadily shifts towards higher angles with decreasing RH, whereas higher-order reflections are systematically visible at 4.7-4.8 Å and 3.15-3.20 Å. In addition, a low-angle reflection is visible, its position shifting from ~22.5 to ~17 Å when RH decreases from 95 to 45% (arrows in Fig. 2A). Similar to Zn-stev, Mg-stev d_{001} increases to ~17 Å upon EG solvation, as expected for smectite (Fig. 2B). Positions of higher-order reflections (at ~9.8, 5.67, and 3.35 Å) indicate however the possible interstratification with non-expandable or collapsed layers. By contrast, XRD patterns of Mg-sap and Mg-hect displays two series of almost rational 00*l* reflections after EG solvation, both corresponding to layer-to-layer distances of ~16.9 Å (Fig. 2B).

When plotting the full width at half maximum intensity (FWHM) of the first basal reflection as a function of its position (Fig. 3), one may note the significant broadening of Zn-smectite basal reflections compared to their Mg equivalents, except for stevensite. This increase in FWHM is most likely related to the lower crystallinity of Zn smectite in relation to their lower synthesis temperature (170-220 °C compared to 300-400 °C for Mg-smectites). In all cases, XRD peak breadth is positively correlated to specific surface area values (Table 1), evidencing the major influence of crystallinity on both values. Compared to Mg-sap and Mg-

hect, crystallinity of Mg-stev is significantly degraded owing to the lower synthesis temperature and duration (400 °C for 1 month for Mg-hect and Mg-sap compared to 300 °C for 2 weeks for Mg-stev). In addition, FWHM is minimal for Mg-sap and Mg-hect for apparent d_{001} values of ~15.5 and ~12.4 Å, that correspond to typical layer-to-layer distances of 2W and 1W smectites (Bradley *et al.*, 1937; Norrish, 1954a; Ferrage *et al.*, 2010; Dazas *et al.*, 2013). These minimal FWHM values correspond to optimal hydration homogeneity with about 90% of the layers or more having the same hydration state (Ferrage *et al.*, 2005b; Aristilde *et al.*, 2013). On this plot, FWHM values determined for Mg-hect are systematically higher than the ones determined for Mg-sap and Mg-hect. This is possibly related to the lower temperature used for the synthesis of the former sample (300 °C compared to 400 °C for Mg-sap and Mg-hect). One may note however that FWHM values of Mg-stev are decreasing as its apparent d_{001} value is decreasing to match the typical layer-to-layer distance of 0W Na-saturated smectite (9.6 Å), as a possible indication of decreased hydration heterogeneity. Consistent with Mg-sap and Mg-hect, the three Zn-smectites exhibit minimal values of FWHM for $d_{001} \approx$ 15.5 Å (Fig. 3 – triangles). A second minimum for $d_{001} \approx$ 12.4 Å is observed only for Zn-sap, however, FWHM values steadily decreasing for both Zn-hect and Zn-stev for d_{001} values lower than ~14.5 Å. For Zn-stev, FWHM values actually come to a minimum for $d_{002} \approx$ 11.0-11.3 Å (dotted-dashed ellipse in Fig. 3), that possibly corresponds to the second-order of the low-angle maximum. Similar low FWHM values are observed when Zn-stev is fully dehydrated ($d_{001} \leq$ 10.0 Å).

Water vapor desorption isotherms

The comparison of H_2O vapor desorption isotherms obtained for stevensite and for their hectorite/saponite counterparts shows that, for a given chemistry (i.e. for Zn- and Mg-smectites), H_2O contents are similar for both hectorite and saponite, whereas H_2O content is decreased by ~2.0-2.5 mmol g^{-1} in stevensite (Fig. 4). For example, at 30% RH, both Mg- and Zn-stev accommodate ~2.0 mmol H_2O per g of dry clay whereas the saponite and hectorite equivalent host ~5 and ~4 mmol H_2O per g of dry clay (Mg- and Zn-smectites, respectively). The different H_2O contents determined for Zn- and Mg-sap/hect essentially result from the difference in molecular weights for the two chemical compositions.

In addition, the transition between the two plateaus corresponding to 1W and 2W hydration states (4-7 and 10-14 mmol H_2O per g of dry clay, respectively, for Mg-sap/hect –

gray areas in Fig. 4) differs significantly from hectorite and saponite on the one hand and stevensite on the other hand. For Mg-smectites, the transition spreads from ~60 to ~40% RH for both saponite and hectorite whereas no transition is visible for stevensite, consistent with the almost constant position of the first basal reflection at ~10.2 Å. For Zn-smectites, the transition appears smoother than for Mg-smectites, possibly as the result of the lower crystallinity and synthesis temperature (Table 1 – Michot *et al.*, 2005). Compared to Mg-smectites, this 2W-to-1W transition also appears shifted to lower RH values and spreads from ~50% to ~35% RH. In contrast to Mg-smectites, the transition is visible for all three Zn smectite varieties, including Zn-stev, although Zn-stev seems to exhibit no stable 1W hydration state.

X-ray diffraction profile modeling

XRD profile modeling allows gaining additional insights into the hydration behavior of stevensite relative to other trioctahedral smectite varieties (saponite and hectorite). The lower temperatures used to synthesize stevensite, compared to saponite/hectorite, strongly degrade the crystallinity of the synthetic smectite product. As a consequence, the intensity and resolution of high-angle reflections are lowered thus hampering the determination of interlayer H_2O structure. The relative proportions of the different smectite hydration states coexisting at a given relative humidity can be deduced however from the modeling of the low-angle region (2-30 °2θ Cu Kα). Fits to the data are provided as supplementary information (Figs SI1, SI3-SI4) together with the composition of the different contributions to the calculated diffraction patterns (Tables SI1-SI3).

Compared to Mg-sap/hect (Ferrage *et al.*, 2010; Dazas *et al.*, 2015; Vinci *et al.*, 2020), hydration appears much more heterogeneous in Zn-smectites (Fig. 5; Tables SI1-SI3).The proportion of a given hydration state (0W, 1W, 2W, or 3W) never exceeds 75%, except for dehydrated layers in Zn-stev for RH conditions below 25% RH (Fig. 5). This increased heterogeneity is possibly linked to an increased chemical heterogeneity in relation to lower synthesis temperature. This effect is likely enhanced by the decrease in crystallinity that smoothens the transition between defined hydration states (Michot *et al.*, 2005). In apparent contradiction with H_2O vapor desorption isotherms, prevalence of 1W layers over 2W layers initiates at higher RH conditions for Zn-smectites (60-50% and 70-60% RH for Zn-sap and Zn-hect, respectively), compared to their Mg equivalent. Zn-stev dehydration occurs even at

higher humidity conditions as the proportions of 2W Zn-stev layers is null at 50% RH and below, whereas Zn-sap and Zn-hect still contain ~35 and 25%, respectively, of 2W layers at 50% RH. Similarly, 0W layers prevail in Zn-stev from 60% RH down to 0% RH, whereas these layers prevail only at 10% RH in Zn-hect (Fig. 5). It is noteworthy that 1W layers never prevail in Zn-stev, whatever the RH conditions, consistent with the absence of a FWHM minimum corresponding to a layer-to-layer distance typical for this hydration state (Fig. 3). Although 1W layers prevail in Zn-hect from 65% to 15%RH, the relative proportions of these layers never exceeds ~60%, the high hydration heterogeneity being in this case responsible for the absence of a FWHM minimum corresponding to a layer-to-layer distance typical for 1W layers (Fig. 3).

Finally, fitting the low-angle maximum of both Zn-stev and Mg-stev required a contribution from a regular 1:1 interstratification of 0W and 1W layers (Fig. SI5, Table SI1). This ordered interstratification allowed fitting the low-angle reflection at 20-22 Å, consistent with previous reports and hypotheses (Brindley, 1955; Faust *et al.*, 1959; Shimoda, 1971), although interstratification implied 0W and 1W layers rather than 0W and 2W, as previously hypothesized. The presence, and major contribution, of this regular interstratification (mixed-layer #4 in Table SI1) also accounts for the minimum FWHM observed in the XRD patterns of Zn-stev in which the position of the first basal reflection is 11.0-11.3 Å (Fig. 3).

Swelling ability and stevensite identification

To differentiate stevensite from other trioctahedral smectites (saponite/hectorite) Christidis and Koustopoulou (2013) proposed to saturate smectites with EG after heating to 500 °C. Upon this dual treatment, saponite and hectorite expand whereas stevensite layers remain collapsed. The criterion proposed by these authors appear valid for Mg-hect and Mg-stev, the former re-expanding almost completely to ~17 Å after heating to 350 °C and EG solvation whereas Mg-stev remains essentially collapsed to ~9.6 Å (Fig. 6A). By contrast, both Zn-stev and Zn-hect do not re-expand after the same treatment whereas Zn-sap swelling ability is essentially unaffected (Fig. 6B). The origin of the contrasting swelling behavior observed for hectorite depending on its octahedral composition remains unexplained but pleads for additional investigation to assess the validity of identification criterion proposed by Christidis and Koustopoulou (2013). In particular, it is necessary to assess the influence i) of crystallinity on smectite hydration behavior, ii) of the octahedral composition on the hectorite ability to re-expand upon heating and EG solvation, and iii) of the possible layer heterogeneity resulting

from the presence of stevensite- and talc-like domains/layers in synthetic smectites (Christidis *et al.*, 2018).

Conclusion

For a given layer charge (~0.8 e^- per $O_{20}(OH)_4$ in the present study) and chemical composition, the H_2O content is lower (by ~2.0 mmol H_2O per g of dry clay) in stevensite compared to its hectorite and saponite equivalents. As a result of this lower H_2O content, the transition from prevailing 2W to prevailing 1W hydration states occurs at slightly higher RH values for Zn-stev compared to Zn-sap and Zn-hect. Hydration behavior of Zn-sap and Zn-hect is similar to that of their Mg counterparts. In addition, 1W layers never prevail in Zn-stev, whatever the H_2O activity, the position of its first basal reflection shifting steadily from an apparent d_{001} of 15.5 Å, consistent with the prevalence of 2W layers, to ~9.6 Å, consistent with Zn-stev complete dehydration. Dehydrated layers prevail in Zn-stev from 60% RH down to 0% RH. Finally, the low-angle reflection commonly observed for stevensite under air-dried conditions is due to the presence of the regular interstratification of 0W and 1W layers.

With respect to stevensite identification from X-ray diffraction of heated and EG-solvated samples (Christidis & Koutsopoulou, 2013), the chemical composition of the octahedral sheet (Zn or Mg in the present study) appears to strongly modify hectorite swelling behavior, thus challenging the method. Further research is needed to decipher the origin of this effect and to propose a more general identification method.

Acknowledgments

DV thanks U. Bari from granting her a Ph.D. fellowship. The CNRS interdisciplinary défi Needs, through its “MiPor” program, is thanked for the financial support to the present study. ISTerre is part of Labex OSUG@2020 (ANR10 LABX56).

References

Aristilde L., Lanson B. & Charlet L. (2013) Interstratification patterns from the pHh-dependent intercalation of a tetracycline antibiotic within montmorillonite layers. *Langmuir*, **29**, 4492-4501.

Bentz J.L. & Peterson R.C. (2020) The formation of clay minerals in the mudflats of Bolivian salars. *Clays and Clay Minerals*, **68**, 115-134.

Bergaoui L., Lambert J.-F., Franck R., Suquet H. & Robert J.-L. (1995) Al-pillared saponites. Part 3.—effect of parent clay layer charge on the intercalation–pillaring mechanism and structural properties. *Journal of the Chemical Society, Faraday Transactions*, **91**, 2229-2239.

Bradley W.F., Grim R.E. & Clark G.F. (1937) A study of the behavior of montmorillonite upon wetting. *Zeitschrift für Kristallographie*, **97**, 216-222.

Brindley G.W. (1955) Stevensite, a montmorillonite-type mineral showing mixed-layer characteristics. *American Mineralogist*, **40**, 239-247.

Brindley G.W. (1980) Order-disorder in clay mineral structures. Pp. 125-195. In G.W. Brindley, and G. Brown, Eds. *Crystal structures of clay minerals and their X-ray identification*, Mineralogical Society, London.

Christidis G.E. & Koutsopoulou E. (2013) A simple approach to the identification of trioctahedral smectites by X-ray diffraction. *Clay Minerals*, **48**, 687-696.

Christidis G.E., Aldana C., Chryssikos G.D., Gionis V., Kalo H., Stöter M., Breu J. & Robert J.-L. (2018) The nature of laponite: Pure hectorite or a mixture of different trioctahedral phases? *Minerals*, **8**, 314.

Dazas B., Lanson B., Breu J., Robert J.L., Pelletier M. & Ferrage E. (2013) Smectite fluorination and its impact on interlayer water content and structure: A way to fine tune the hydrophilicity of clay surfaces? *Microporous and Mesoporous Materials*, **181**, 233-247.

Dazas B., Lanson B., Delville A., Robert J.-L., Komarneni S., Michot L.J. & Ferrage E. (2015) Influence of tetrahedral layer charge on the organization of interlayer water and ions in synthetic Na-saturated smectites. *The Journal of Physical Chemistry C*, **119**, 4158-4172.

de Oliveira Nardi Leite C., de Assis Silva C.M. & de Ros L.F. (2020) Depositional and diagenetic processes in the pre-salt rift section of a Santos basin area, SE Brazil. *Journal of Sedimentary Research*, **90**, 584-608.

Drits V.A. & Tchoubar C. (1990) *X-ray diffraction by disordered lamellar structures: Theory and applications to microdivided silicates and carbons*. Pp. 371. Springer-Verlag, Berlin.

Eberl D.D., Jones B.F. & Khoury H.N. (1982) Mixed-layer kerolite/stevensite from the Amargosa desert, Nevada. *Clays & Clay Minerals*, **30**, 321-326.

Faust G.T., Hathaway J.C. & Millot G. (1959) A restudy of stevensite and allied minerals. *American Mineralogist*, **44**, 342-370.

Ferrage E., Lanson B., Malikova N., Plancon A., Sakharov B.A. & Drits V.A. (2005a) New insights on the distribution of interlayer water in bi-hydrated smectite from X-ray diffraction profile modeling of 00l reflections. *Chemistry of Materials*, **17**, 3499-3512.

Ferrage E., Lanson B., Sakharov B.A. & Drits V.A. (2005b) Investigation of smectite hydration properties by modeling experimental X-ray diffraction patterns: Part I. Montmorillonite hydration properties. *American Mineralogist*, **90**, 1358-1374.

Ferrage E., Lanson B., Michot L.J. & Robert J.L. (2010) Hydration properties and interlayer organization of water and ions in synthetic Na-smectite with tetrahedral layer charge. Part 1. Results from X-ray diffraction profile modeling. *The Journal of Physical Chemistry C*, **114**, 4515-4526.

Ferrage E., Sakharov B.A., Michot L.J., Delville A., Bauer A., Lanson B., Grangeon S., Frapper G., Jimenez-Ruiz M. & Cuello G.J. (2011) Hydration properties and interlayer organization of water and ions in synthetic Na-smectite with tetrahedral layer charge. Part 2. Towards a precise coupling between molecular simulations and diffraction data. *The Journal of Physical Chemistry C*, **115**, 1867-1881.

Hamilton D.L. & Henderson C.M.B. (1968) The preparation of silicate compositions by a gelling method. *Mineralogical Magazine*, **36**, 832-838.

Higashi S., Miki K. & Komarneni S. (2002) Hydrothermal synthesis of Zn-smectites. *Clays and Clay Minerals*, **50**, 299-305.

Jones B.F. (1986) Clay mineral diagenesis in lacustrine environments. Pp. 291-300. In F.A. Mumpton, Ed. *Studies in diagenesis*.

Khoury H.N., Eberl D.D. & Jones B.F. (1982) Origin of magnesium clays from the Amargosa desert, Nevada. *Clays & Clay Minerals*, **30**, 327-336.

Laird D.A., Barak P., Nater E.A. & Dowdy R.H. (1991) Chemistry of smectitic and illitic phases in interstratified soil smectite. *Soil Science Society of America Journal*, **55**, 1499-1504.

Malikova N., Cadene A., Marry V., Dubois E., Turq P., Zanotti J.M. & Longeville S. (2005) Diffusion of water in clays - microscopic simulation and neutron scattering. *Chemical Physics*, **317**, 226-235.

Malikova N., Cadene A., Dubois E., Marry V., Durand Vidal S., Turq P., Breu J., Longeville S. & Zanotti J.M. (2007) Water diffusion in a synthetic hectorite clay studied by quasi-elastic neutron scattering. *The Journal of Physical Chemistry C*, **111**, 17603-17611.

Michot L.J., Bihannic I., Pelletier M., Rinnert E. & Robert J.L. (2005) Hydration and swelling of synthetic Na-saponites: Influence of layer charge. *American Mineralogist*, **90**, 166-172.

Michot L.J., Delville A., Humbert B., Plazanet M. & Levitz P. (2007) Diffusion of water in a synthetic clay with tetrahedral charges by combined neutron time-of-flight measurements and molecular dynamics simulations. *The Journal of Physical Chemistry C*, **111**, 9818-9831.

Michot L.J., Ferrage E., Jiménez-Ruiz M., Boehm M. & Delville A. (2012) Anisotropic features of water and ion dynamics in synthetic Na- and Ca-smectites with tetrahedral layer charge. A combined quasi-elastic neutron-scattering and molecular dynamics simulations study. *The Journal of Physical Chemistry C*, **116**, 16619-16633.

Mooney R.W., Keenan A.G. & Wood L.A. (1952) Adsorption of water by montmorillonite. II. Effect of exchangeable ions and lattice swelling as measured by X-ray diffraction. *Journal of the American Chemical Society*, **74**, 1371-1374.

Nagelschmidt G. (1936) On the lattice shrinkage and structure of montmorillonite. *Zeitschrift für Kristallographie*, **93**, 481-487.

Norrish K. (1954a) Manner of swelling of montmorillonite. *Nature*, **173**, 256-257.

-. (1954b) The swelling of montmorillonite. *Discussions of the Faraday Society*, **18**, 120-133.

Rinnert E., Carteret C., Humbert B., Fragneto Cusani G., Ramsay J.D.F., Delville A., Robert J.L., Bihannic I., Pelletier M. & Michot L.J. (2005) Hydration of a synthetic clay with tetrahedral charges: A multidisciplinary experimental and numerical study. *The Journal of Physical Chemistry B*, **109**, 23745-23759.

Robert J.L., Beny J.M., Della Ventura G. & Hardy M. (1993) Fluorine in micas: Crystal-chemical control of the OH-F distribution between trioctahedral and dioctahedral sites. *European Journal of Mineralogy*, **5**, 7-18.

Sakharov B.A. & Lanson B. (2013) X-ray identification of mixed-layer structures. Modelling of diffraction effects. Pp. 51-135. In F. Bergaya, and G. Lagaly, Eds. *Handbook of clay science, Part B. Techniques and applications*, Elsevier, Amsterdam.

Shimoda S. (1971) Mineralogical studies of a species of stevensite from the Obori mine, Yamagata prefecture, Japan. *Clay Minerals*, **9**, 185-192.

Thiry M., Milnes A. & Ben Brahim M. (2014) Pleistocene cold climate groundwater silicification, Jbel Ghassoul region, Missour basin, Morocco. *Journal of the Geological Society*, **172**, 125-137.

Vinci D., Dazas B., Ferrage E., Lanson M., Magnin V., Findling N. & Lanson B. (2020) Influence of layer charge on hydration properties of synthetic octahedrally-charged Na-saturated trioctahedral swelling phyllosilicates. *Applied Clay Science*, **184**, 105404.

Tables

Table 1. Specific surface areas determined for Zn- and Mg-smectites with the BET method.

Sample	Specific surface area (m^2/g)
Mg-hect	11.1
Mg-sap	50.1
Mg-stev	179.9
Zn-hect	146.9
Zn-sap	96.7
Zn-stev	100.7

Figure captions

Fig. 1. (A) X-ray diffraction patterns of Zn-stev along the H_2O vapor desorption isotherm. (B) X-ray diffraction patterns of Zn-sap, Zn-hect, and Zn-stev collected at 20% RH (black lines), 70% RH (blue lines), and upon EG solvation (red lines). Dotted lines in (A) indicate the typical positions of the first basal reflection for different smectite hydration states, arrows indicating the position of low-angle reflection. Hal. Indicates the presence of halite. The vertical gray bar indicates a modified scale factor for the high-angle region compared to the 2-15 °2θ range.

Fig. 2. (A) X-ray diffraction patterns of Mg-stev along the H_2O vapor desorption isotherm. (B) X-ray diffraction patterns of Mg-sap, Mg-hect, and Mg-stev collected at 20% RH (black lines), 70% RH (blue lines), and upon EG solvation (red lines). Dotted lines in (A) indicate the typical positions of the first basal reflection for different smectite hydration states, arrows indicating the position of low-angle reflection. Hal. Indicates the presence of halite. The vertical gray bar indicates a modified scale factor for the high-angle region compared to the 2-15 °2θ range s.

Fig. 3. Evolution of the full-width at half-maximum intensity (FWHM) of the first basal reflection as a function of its position for Zn- and Mg-smectites (triangles and circles, respectively). Data for Mg-smectites from Ferrage *et al.* (2010), Dazas *et al.* (2013), and Vinci *et al.* (2020). The dashed ellipses highlight minimum FWHM values corresponding to essentially homogeneous 1W and 2W hydration states. Position of the first basal reflection essentially decreases with decreasing RH conditions during data collection from an initial "wet" state at 90-95% RH depending on the sample..

Fig. 4. Water content as a function of relative humidity along the water vapor desorption isotherms. Dotted and solid lines represent Mg- and Zn-smectites, respectively. Mg-sap and Mg-hect data from (Ferrage *et al.*, 2010) and (Dazas *et al.*, 2013), respectively. Gray areas indicate the 1W and 2W plateaus occurring for Mg-sap/hect.

Fig. 5. Evolution of the relative proportions of the different layer types (summing up all contributions to the diffracted intensity) along H_2O vapor desorption isotherms for Zn-stev, Zn-hect, and Zn-sap.

Fig. 6. Comparison of X-ray diffraction patterns obtained after EG solvation (red) and heating to 350 °C followed by EG solvation (black). (A) Mg-smectites: Mg-hect (dashed lines), and Mg-stev (dotted-dashed lines). (B) Zn-smectite: Zn-sap (solid lines), Zn-hect (dashed lines), and Zn-stev (dotted-dashed lines). The vertical gray bar indicates a modified scale factor for the high-angle region compared to the 2-12 °2θ range.

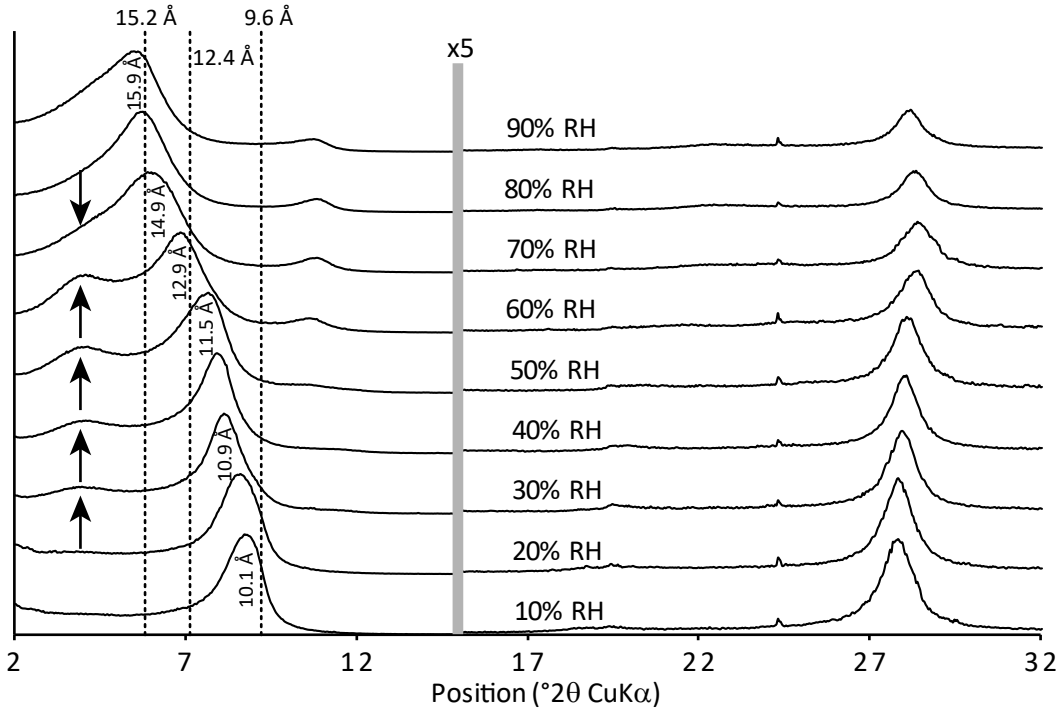

Vinci et al., Fig. 01A

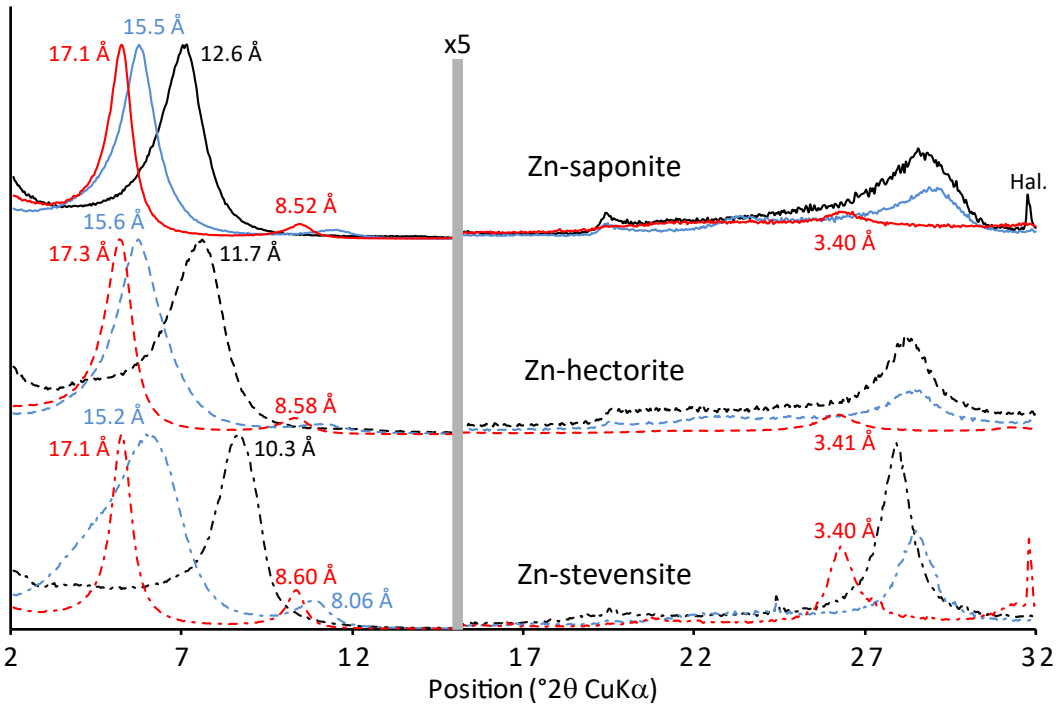

Vinci et al., Fig. 01B

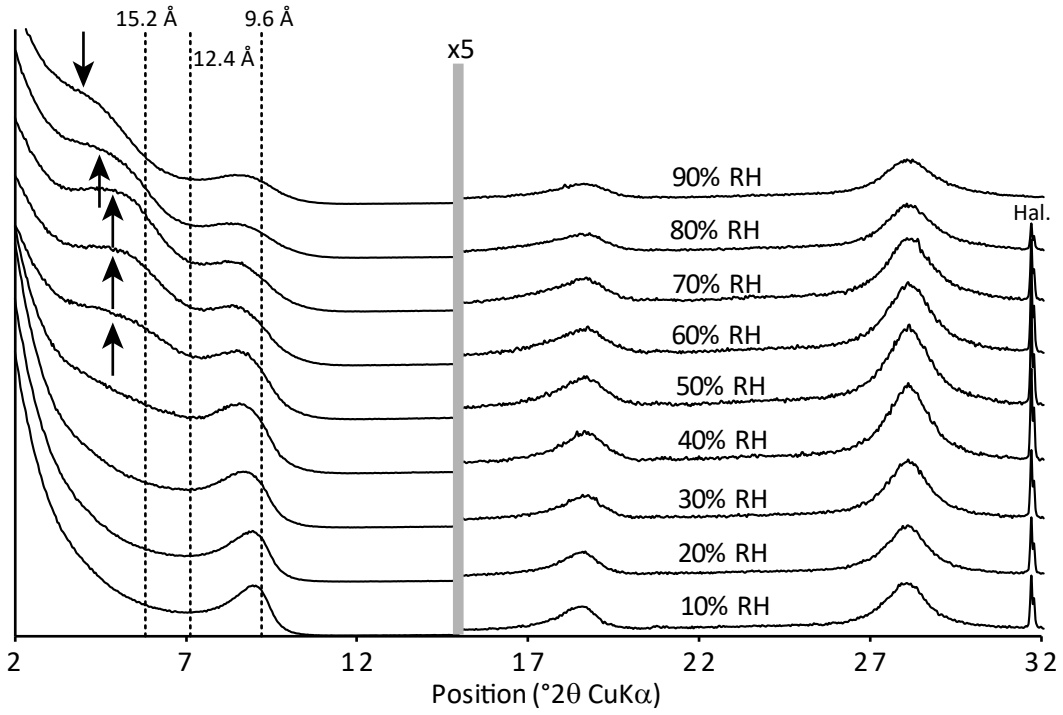

Vinci et al., Fig. 02A

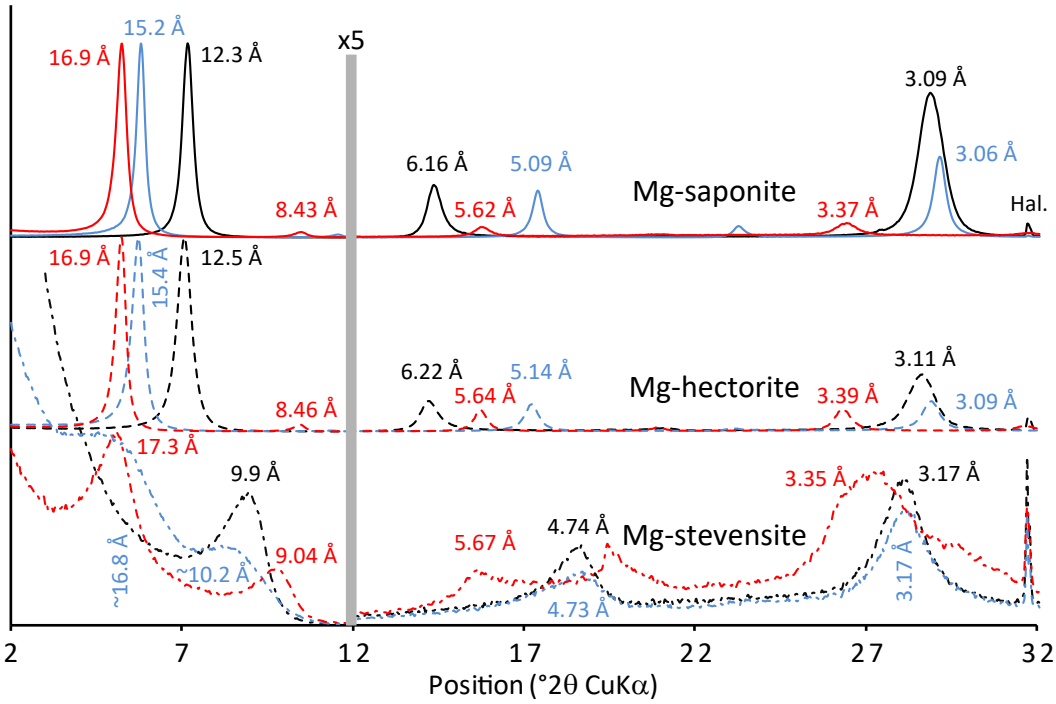

Vinci et al., Fig. 02B

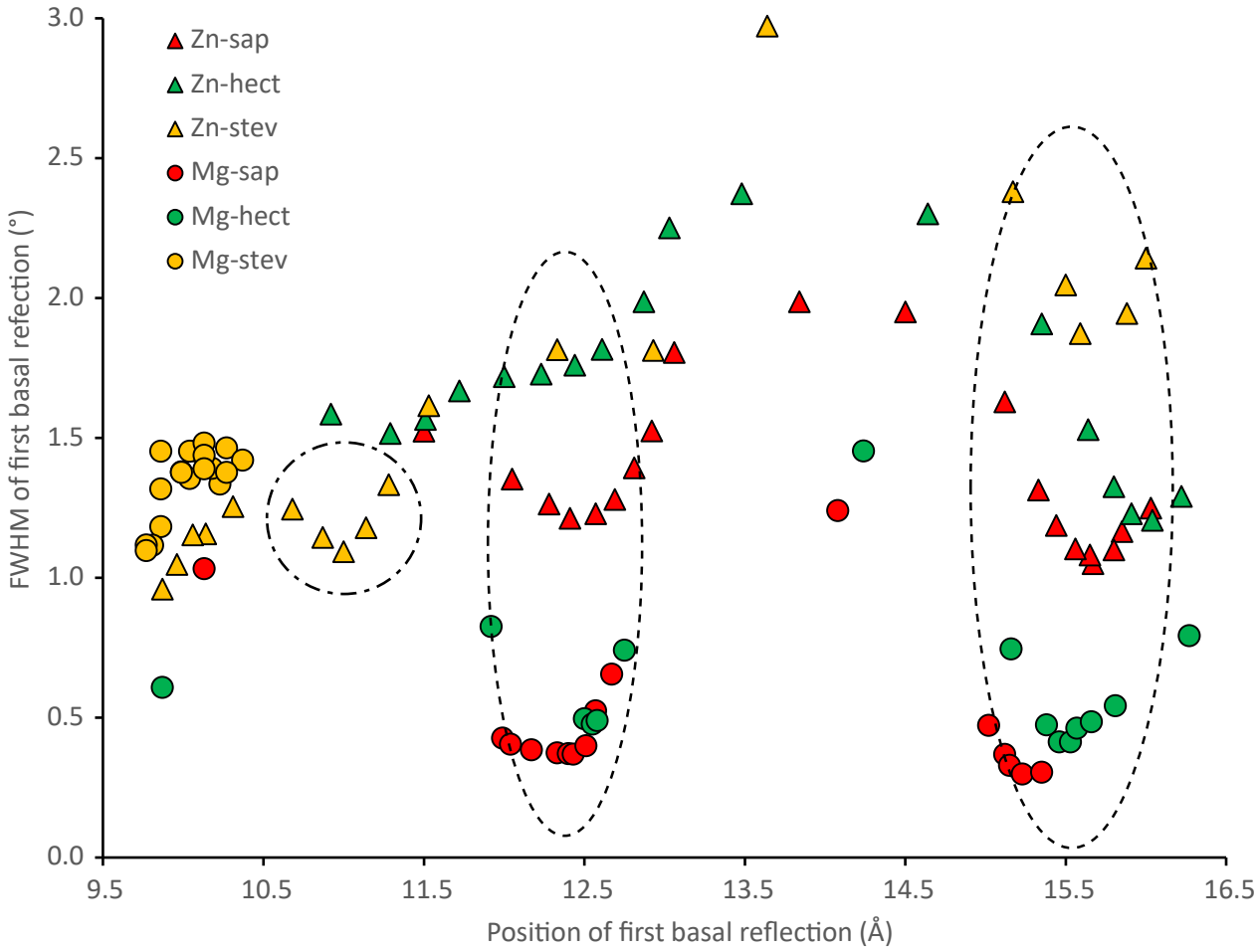

Please insert as a 2 column figure

Vinci et al., Fig. 03

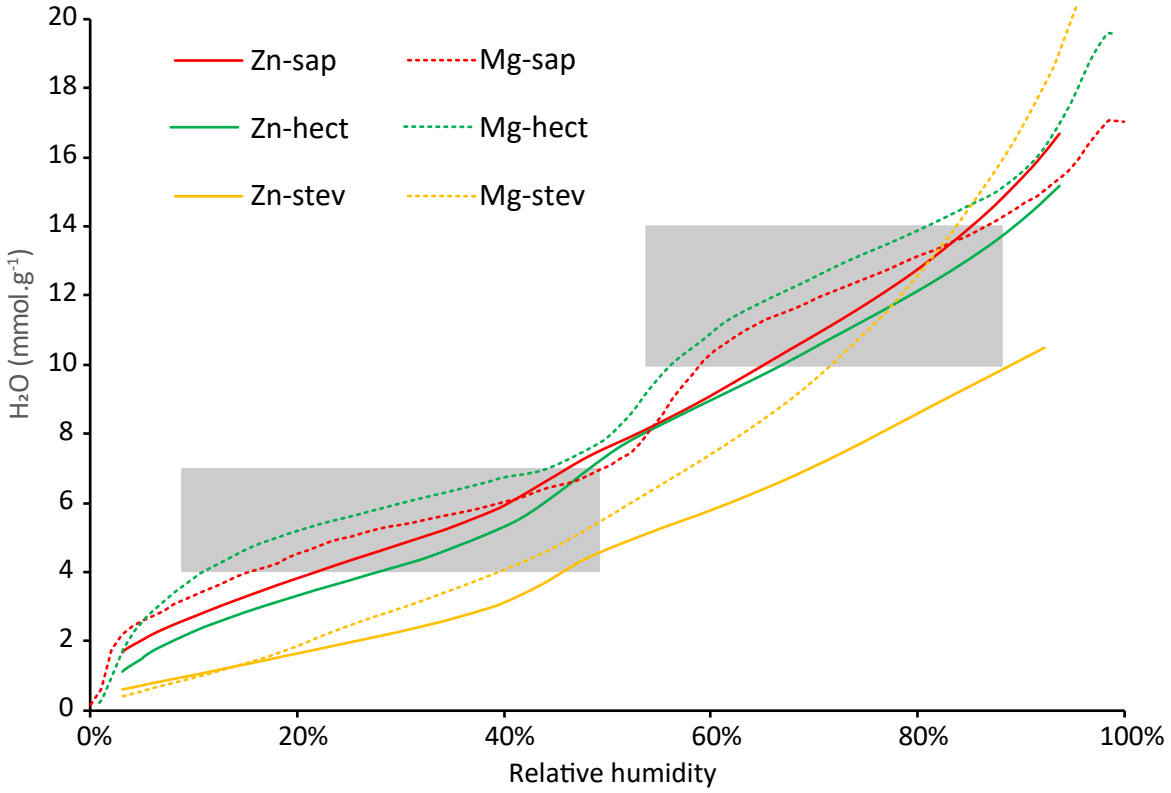

Vinci et al., Fig. 04

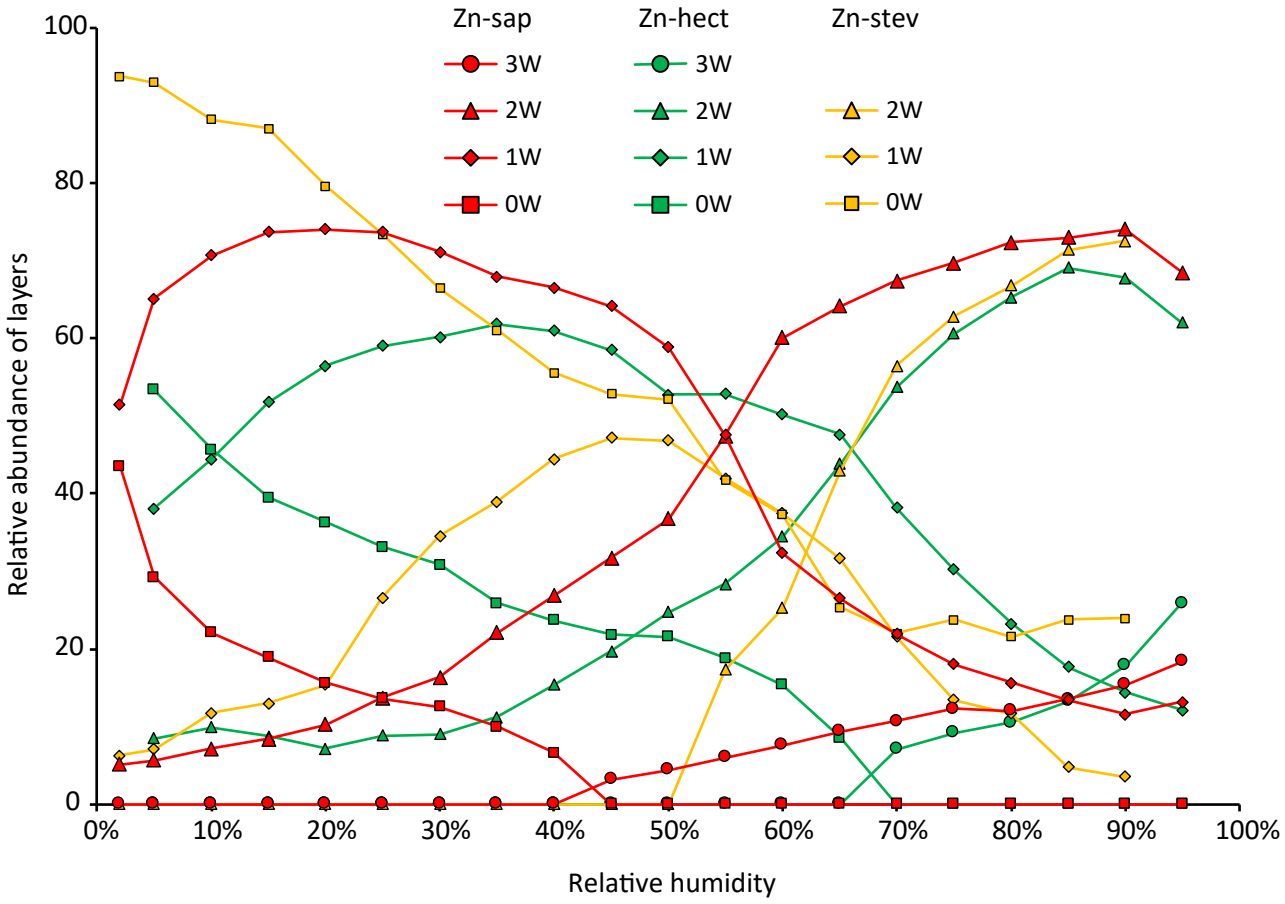

Vinci et al., Fig. 05

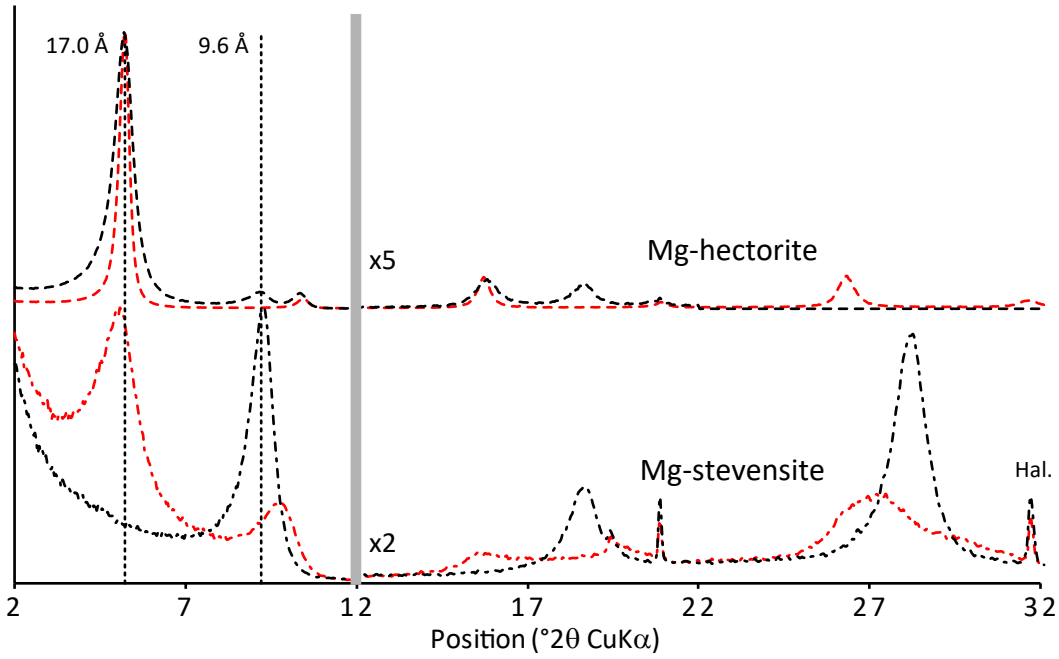

Vinci et al., Fig. 06A

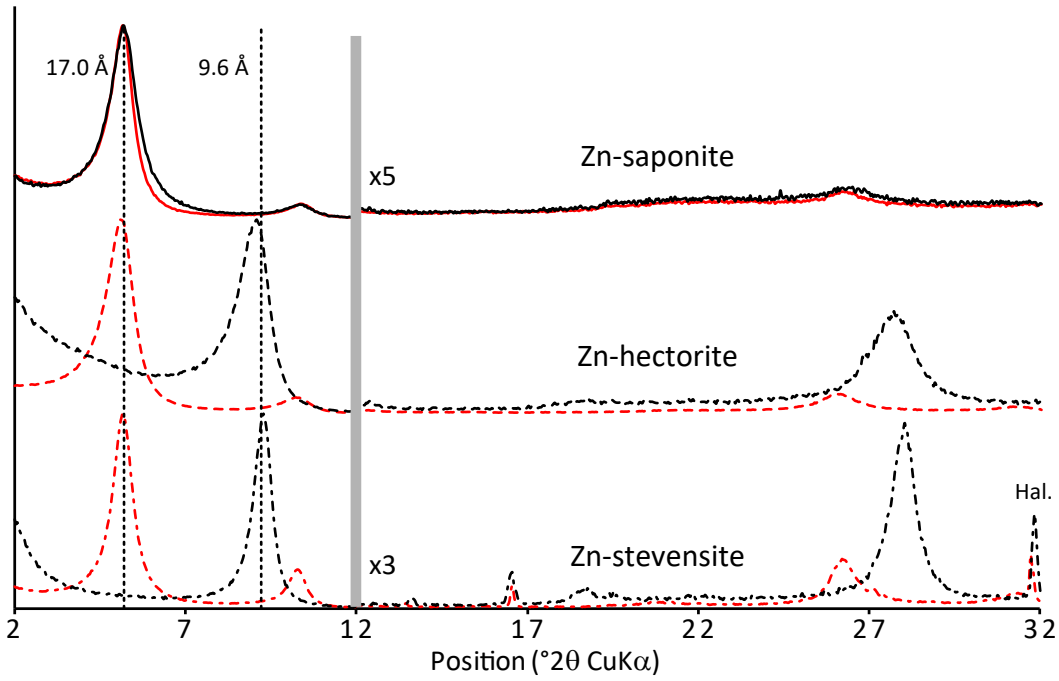

Vinci et al., Fig. 06B

Hydration of Na-saturated Synthetic Stevensite, a Peculiar Trioctahedral Smectite

Doriana Vinci[1,2], Bruno Lanson[1,*], Martine Lanson[1], Valérie Magnin[1], Nathaniel Findling[1]

Univ. Grenoble Alpes, Univ. Savoie Mont Blanc, CNRS, IRD, Univ. Gustave Eiffel, ISTerre, F-38000 Grenoble, France

Dipartimento Scienze Terra & Geoambientali, Univ. Bari Aldo Moro, Bari, Italy

Running title: Hydration of Na-saturated Synthetic Stevensite

*. Corresponding author: bruno.lanson@univ-grenoble-alpes.fr

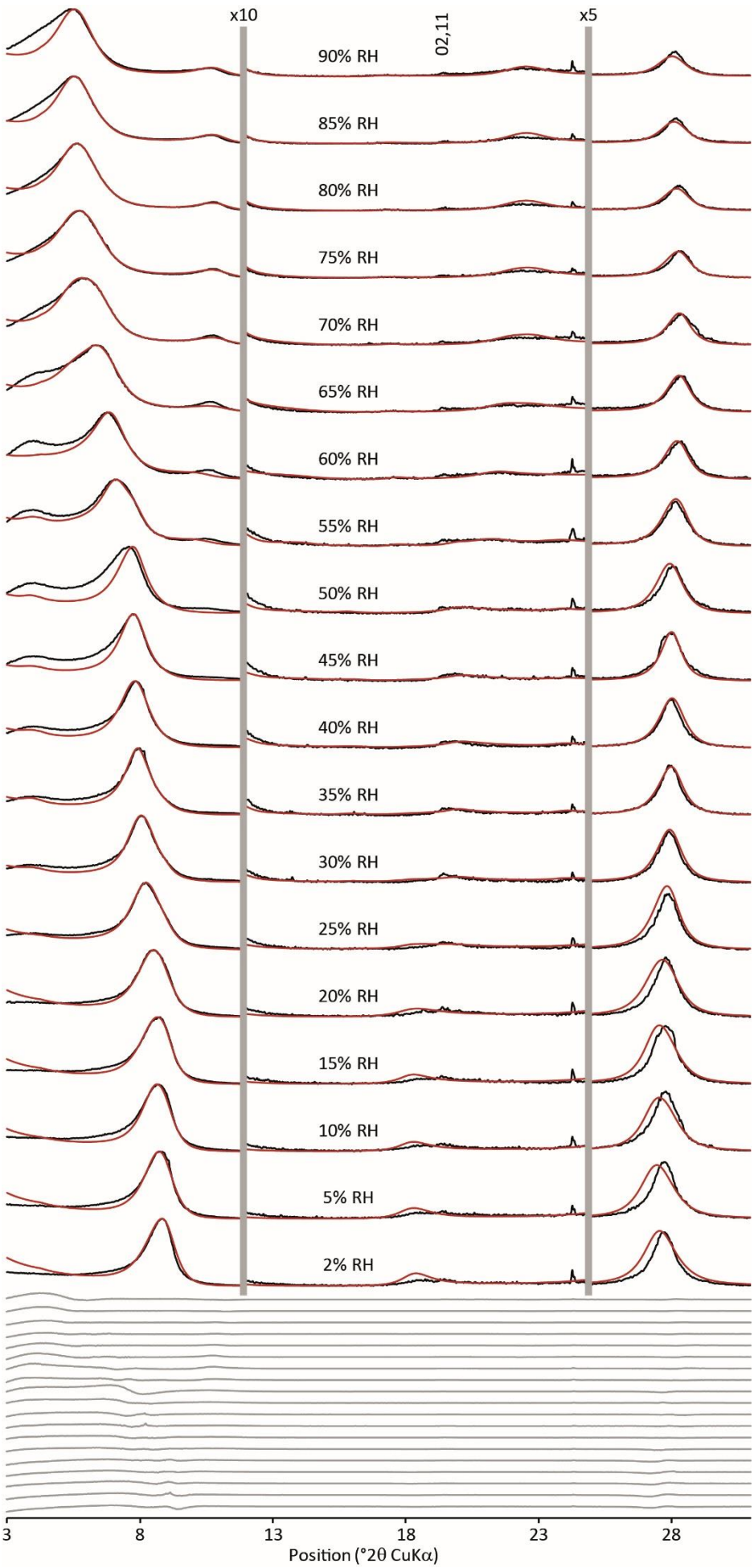
x10
02,11
x5
90% RH
85% RH
80% RH
75% RH
70% RH
65% RH
60% RH
55% RH
50% RH
45% RH
40% RH
35% RH
30% RH
25% RH
20% RH
15% RH
10% RH
5% RH
2% RH
3
8
13
18
23
28
Position (°2θ CuKα)

Fig. SI1. Comparison between experimental and calculated XRD patterns along the H_2O vapor desorption isotherm for Zn-stev. Experimental and calculated XRD patterns are shown as solid red and black lines, respectively. Difference plots are shown at the bottom of the figure as gray lines. The vertical gray bar indicates a modified scale factor for the angle region higher to 12° 2θ compared to the 3-12 °2θ angular range. Diffraction lines from halite (NaCl) impurity are indicated as Hal.

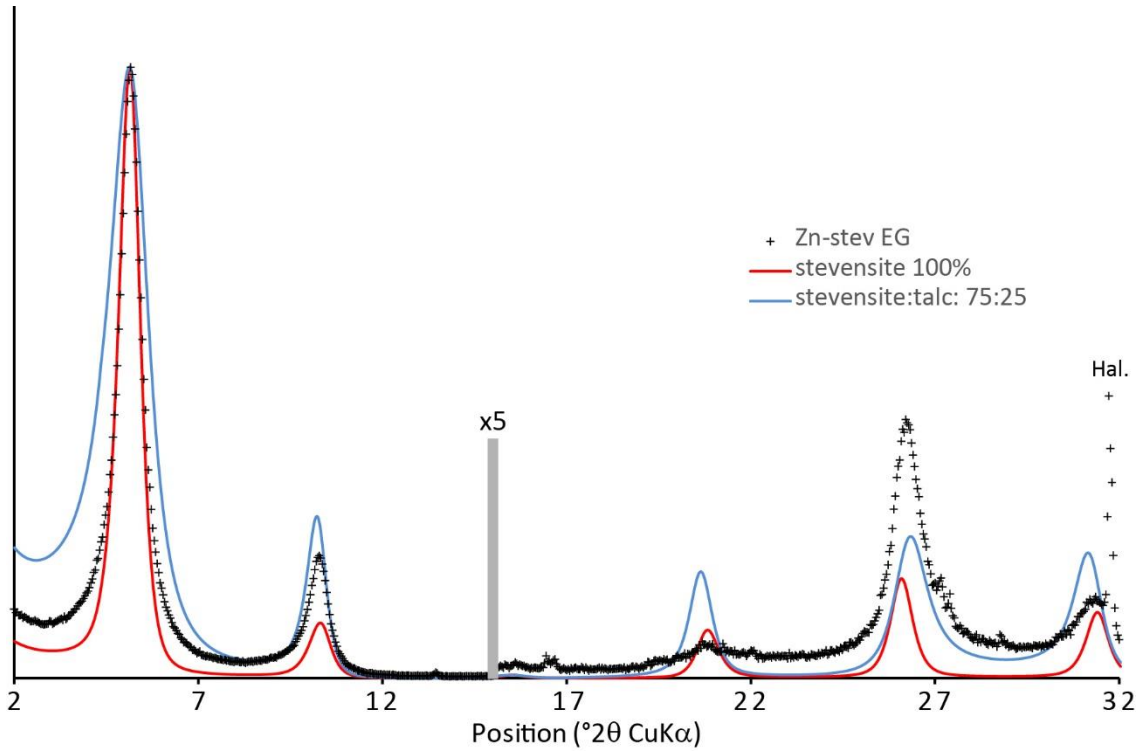

Fig. SI2. Comparison between experimental and calculated XRD patterns for Zn-stev after EG solvation. Experimental data are shown as crosses. Solid red line and blue dashed line correspond to Zn-stev models containing 0 and 25% talc-like layers randomly interstratified with swelling layers. The latter value corresponds to the content of dehydrated (0W) layers in Zn-stev equilibrated at 90% RH (Table SI1). Interlayer model for EG-solvated steventsite layers was not refined from that reported by Moore and Reynolds (1997). The vertical gray bar indicates a modified scale factor for the angle region higher to 15° 2θ compared to the 2-15 °2θ angular range. Diffraction line from halite (NaCl) impurity is indicated as Hal.

Reference cited

Moore D.M. & Reynolds R.C., Jr. (1997) *X-ray diffraction and the identification and analysis of clay minerals*. Pp. 378. Oxford University Press, Oxford.

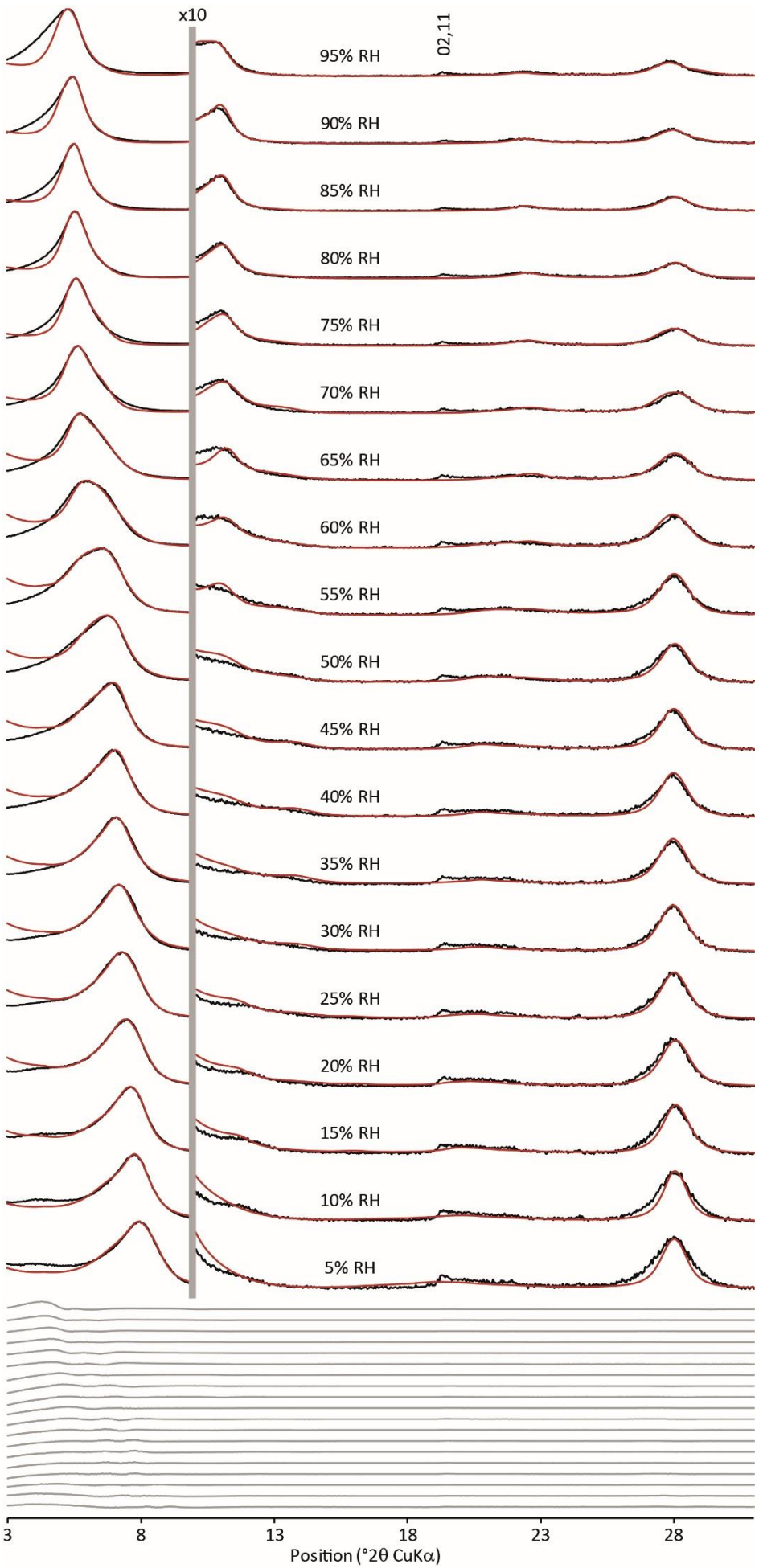
x10
02,11
95% RH
90% RH
85% RH
80% RH
75% RH
70% RH
65% RH
60% RH
55% RH
50% RH
45% RH
40% RH
35% RH
30% RH
25% RH
20% RH
15% RH
10% RH
5% RH
3
8
13
18
23
28
Position (°2θ CuKα)

Fig. SI3. Comparison between experimental and calculated XRD patterns along the H_2O vapor desorption isotherm for Zn-hect. Experimental and calculated XRD patterns are shown as solid red and black lines, respectively. Difference plots are shown at the bottom of the figure as gray lines. The vertical gray bar indicates a modified scale factor for the angle region higher to 10° 2θ compared to the 3-10 °2θ angular range.

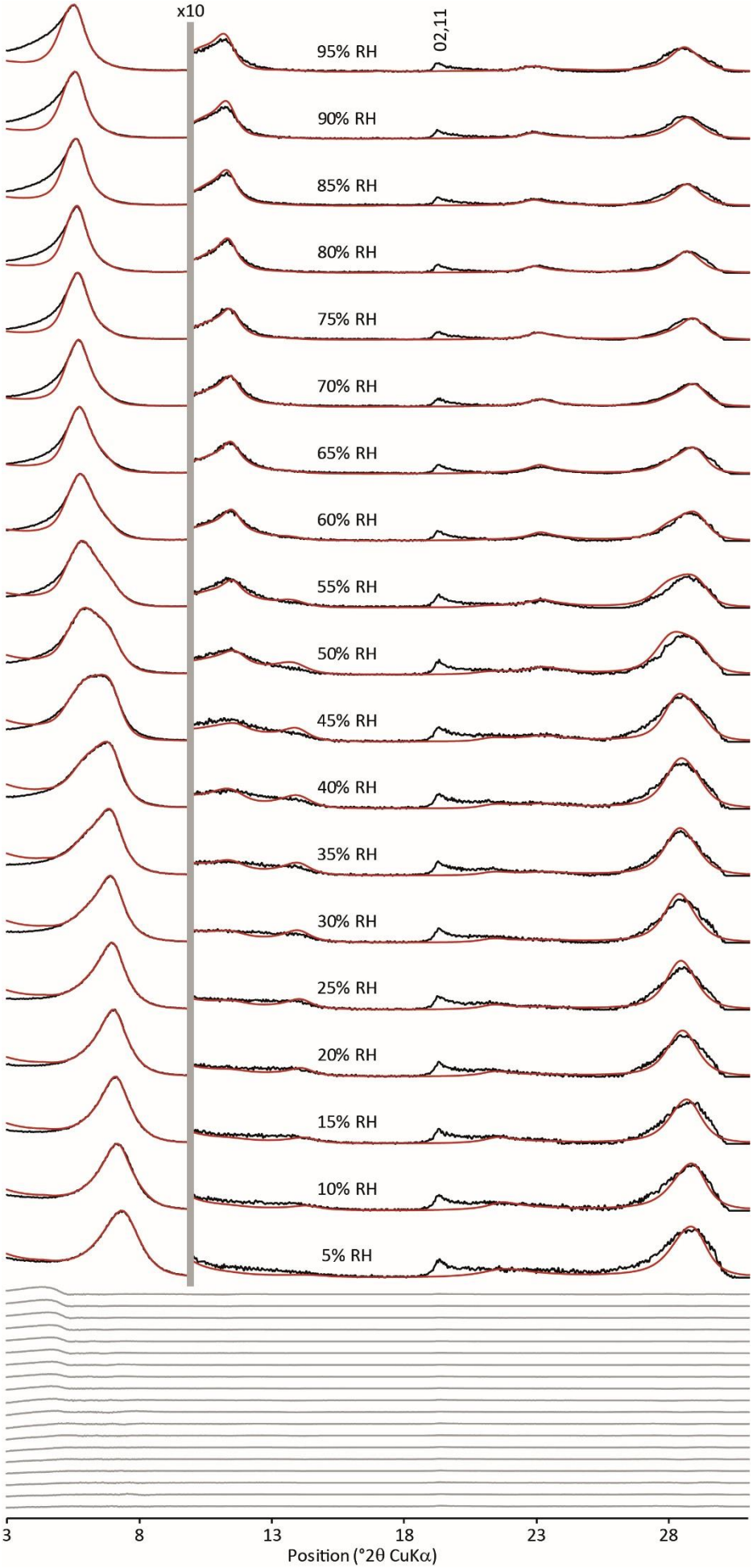
x10
02,11
95% RH
90% RH
85% RH
80% RH
75% RH
70% RH
65% RH
60% RH
55% RH
50% RH
45% RH
40% RH
35% RH
30% RH
25% RH
20% RH
15% RH
10% RH
5% RH
3
8
13
18
23
28
Position (°2θ CuKα)

Fig. SI4. Comparison between experimental and calculated XRD patterns along the H_2O vapor desorption isotherm for Zn-sap. Experimental and calculated XRD patterns are shown as solid red and black lines, respectively. Difference plots are shown at the bottom of the figure as gray lines. The vertical gray bar indicates a modified scale factor for the angle region higher to 10° 2θ compared to the 3-10 °2θ angular range.

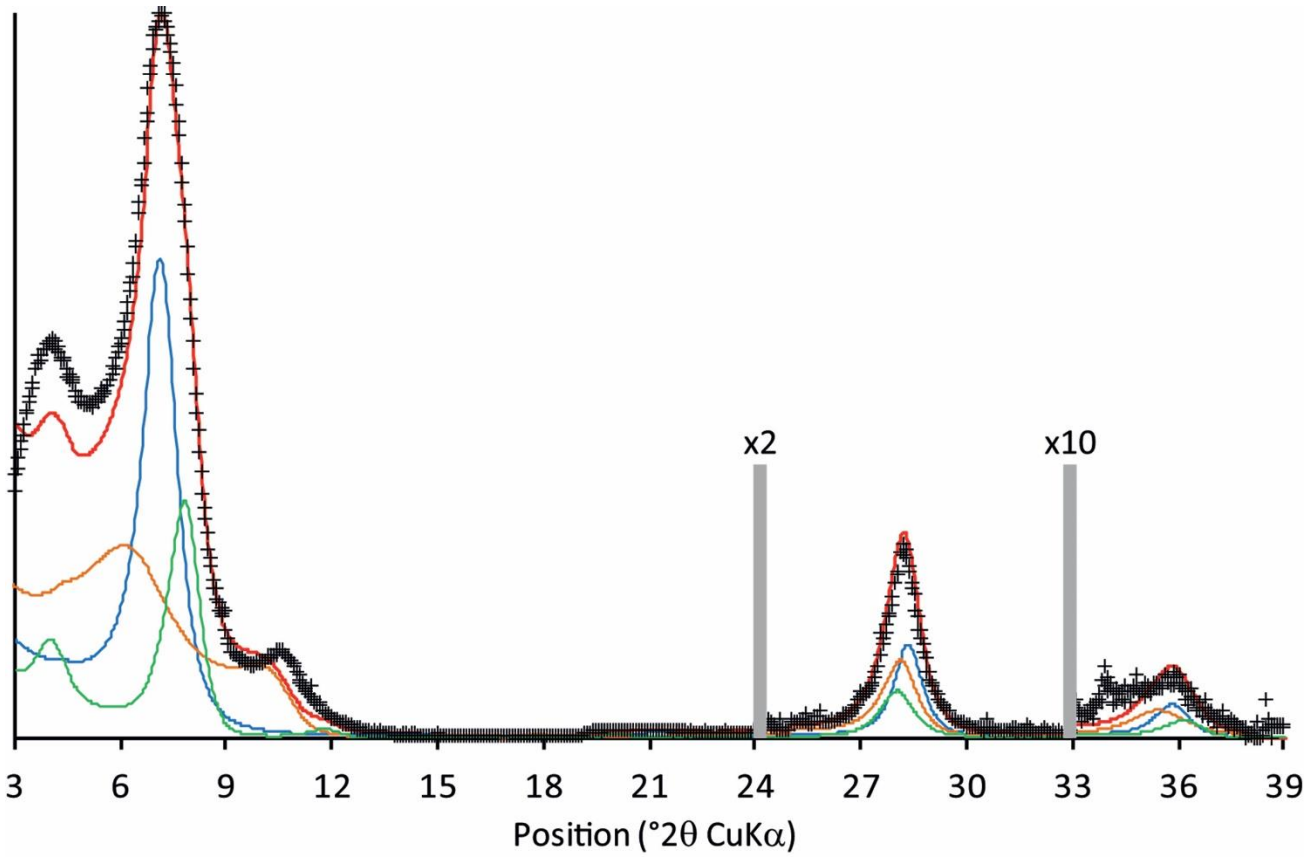

Fig. SI5. Respective contributions of the various mixed layers to the diffraction profile calculated for Zn-stev at 55% RH. Mixed layers #1, #2, and #4 (Table SI1) are shown as solid orange, blue, and green lines, respectively. Optimum fit and diffraction data are shown as solid red line and black crosses, respectively. The vertical gray bars indicate a modified scale factor for the high-angle regions compared to the 2-24 °2θ range.

Table SI1. Structural parameters used to fit experimental XRD patterns of Zn-stev as a function of relative humidity.

	%RH	90	85	80	75	70	65	60	55	50	45	40	35	30	25	20	15	10	5	2
Layer-to-layer distance (in Å)	2W	15.80	15.77	15.73	15.69	15.66	15.63	15.58	15.55											
	1W	12.80	12.70	12.60	12.58	12.57	12.57	12.53	12.53	12.50	12.50	12.45	12.43	12.40	12.40	12.25	12.20	12.10	11.90	11.80
	0W	9.75	9.75	9.75	9.75	9.75	9.75	9.75	9.75	9.75	9.75	9.75	9.75	9.75	9.75	9.75	9.75	9.75	9.75	9.70
Number of H_2O molecules [per $O_{20}(OH)_4$]	2W layers	10.6	10.4	10.0	10.0	9.8	9.6	9.4	9.0	8.8										
	1W layers	4.1	4.1	4.1	4.0	4.0	3.9	3.9	3.9	3.8	3.8	3.7	3.5	3.4	3.0	2.8	2.8	2.5	2.3	1.8
σ_z (in Å)		0.22	0.20	0.22	0.20	0.20	0.20	0.22	0.18	0.18	0.18	0.18	0.18	0.20	0.18	0.15	0.15	0.15	0.15	0.15
σ^* (in °)		4.0	3.8	4.0	3.8	3.5	3.6	3.6	3.0	2.0	3.0	2.4	2.5	2.5	2.0	2.0	2.0	2.0	2.0	2.0
Mixed layer 1	Ab (%)	93	92	79	77	64	48	41	38	3	3	2	2	5	14	20	39	41	53	58
	2W	75	75	75	72	72	65	40	40											
	1W									15	10	10	2	2	2	2	2			
	0W	25	25	25	28	28	35	60	60	85	90	90	98	98	98	98	98	100	100	100
	CSD size (in layers)	4.0	4.0	4.0	4.0	4.0	4.0	8.0	6.0	6.0	7.0	6.0	9.0	9.0	6.0	5.0	6.0	5.5	5.0	5.5
Mixed layer 2	Ab (%)	7	8	12	15	27	43	56	42	80	82	80	81	83	81	75	61	59	47	42
	2W	40	30	25	25	25	20	15	5											
	1W	50	60	60	60	60	60	65	75	48	48	44	38	34	30	20	20	20	15	15
	0W	10	10	15	15	15	20	20	20	52	52	56	62	66	70	80	80	80	85	85
	CSD size (in layers)	5.0	5.0	5.0	5.3	6.0	6.0	6.5	6.0	6.0	9.0	7.0	7.0	9.0	8.0	6.0	6.0	7.0	6.0	5.0
Mixed layer 3	Ab (%)			9	8	9	9	3												
	2W			50	45	40	35	15												
	1W			50	55	60	65	35												
	0W							50												
	CSD size (in layers)			4.2	6.0	7.0	7.0	4.0												
Mixed layer 4 R=1 with maximum possible degree of ordering (MPDO)	Ab (%)								21	16	15	18	17	13	5					
	2W																			
	1W								50	50	50	50	48	48	40					
	0W								50	50	50	50	52	52	60					
	CSD size (in layers)								5.0	5.0	5.0	5.0	7.0	9.0	6.0					

Note: Ab.: Relative abundance; CSD: coherent scattering domain; σ_z: fluctuation of the layer-to-layer distance (in Å); σ^*: orientation parameter(in °)

Table SI2. Structural parameters used to fit experimental XRD patterns of Zn-hect as a function of relative humidity.

	%RH	95	90	85	80	75	70	65	60	55	50	45	40	35	30	25	20	15	10	5
Layer-to-layer distance (in Å)	3W	18.0	18.0	18.0	18.0	18.0	18.0													
	2W	15.88	15.80	15.74	15.70	15.67	15.62	15.60	15.56	15.55	15.52	15.50	15.48	15.47	15.46	15.45	15.43	15.42	15.40	15.38
	1W	13.00	12.98	12.96	12.95	12.95	12.90	12.85	12.75	12.68	12.66	12.65	12.64	12.63	12.61	12.57	12.54	12.49	12.48	12.45
	0W												9.70	9.70	9.70	9.70	9.70	9.70	9.70	9.70
Number of H_2O molecules [per $O_{20}(OH)_4$]	2W layers	11.4	11.2	10.2	9.8	9.6	9.4	9.4	9.2	9.0	8.8	8.0	7.8	7.8	7.8	7.6	7.6	7.2	6.6	6.0
	1W layers	5.6	5.6	5.5	6.0	6.0	5.9	5.8	5.7	5.6	5.4	5.3	5.2	5.1	5.0	4.6	4.2	3.6	2.8	2.3
σ_z (in Å)		0.22	0.24	0.22	0.22	0.22	0.22	0.24	0.22	0.22	0.22	0.22	0.22	0.22	0.22	0.22	0.22	0.22	0.24	0.24
σ^* (in °)		7.0	9.0	9.0	8.0	9.0	7.0	9.0	9.0	9.0	9.0	9.0	8.0	8.0	7.8	7.8	7.5	6.5	7.5	8.0
CSD size (in layers		4.0	4.6	4.8	5.0	5.2	4.5	4.0	4.2	4.5	4.7	5.0	5.0	5.0	5.0	5.0	5.0	6.0	9.0	9.0
Mixed layer 1	Ab (%)	44	57	48	35	30	42	29	27	24	33	41	32	25	20	21	18	23	33	34
	3W	7	6	6	6	6	6													
	2W	90	90	90	90	88	80	95	80	75	55	48	48	45	45	42	40	38	30	25
	1W	3	4	4	4	6	14	5	10	5	23	28	28	31	31	31	33	34	35	35
	0W								10	20	22	24	24	24	24	27	27	28	35	40
Mixed layer 2	Ab (%)	38	24	23	21	20	13	20	36	32	12	3	8	19	20	14	14	15	3	14
	3W	60	60	45	40	37	35													
	2W	40	40	55	60	63	65	5	5	5	10									
	1W							65	65	65	70	75	50	53	45	45	45	45	30	20
	0W							30	30	30	20	25	50	47	55	55	55	55	70	80
Mixed layer 3	Ab (%)	18	16	14	15	21	27	51	37	44	54	56	60	55	60	66	68	62	64	52
	3W																			
	2W	40	30	25	20	20	15	30	30	20	10									
	1W	60	70	75	80	80	85	65	65	70	68	80	80	80	75	70	65	60	50	45
	0W							5	5	10	22	20	20	20	25	30	35	40	50	55
Mixed layer 4	Ab (%)		3	15	28	29	17													
	3W																			
	2W		68	65	65	60	45													
	1W		32	35	35	40	55													
	0W																			

Note: Ab.: Relative abundance; CSD: coherent scattering domain; σ_z: fluctuation of the layer-to-layer distance (in Å); σ^*: orientation parameter(in °)

Table SI3. Structural parameters used to fit experimental XRD patterns of Zn-sap as a function of relative humidity.

	%RH	95	90	85	80	75	70	65	60	55	50	45	40	35	30	25	20	15	10	5
Layer-to-layer distance (in Å)	3W	18.0	18.0	18.0	18.0	18.0	18.0	18.0												
	2W	15.58	15.53	15.52	15.50	15.40	15.38	15.37	15.34	15.32	15.27	15.24	15.23	15.22	15.21	15.16	15.16	15.15	15.15	15.15
	1W	12.82	12.81	12.80	12.80	12.80	12.80	12.79	12.78	12.74	12.70	12.60	12.55	12.55	12.55	12.50	12.46	12.38	12.29	12.24
	0W												9.70	9.70	9.70	9.70	9.70	9.70	9.70	9.70
Number of H_2O molecules [per $O_{20}(OH)_4$]	2W layers	11.0	10.4	10.0	9.4	8.8	8.6	8.4	8.2	8.0	8.0	7.8	7.6	7.4	7.0	6.8	6.6	6.0	4.4	4.0
	1W layers	5.7	5.6	5.5	5.5	5.3	5.7	5.7	5.7	5.6	5.5	5.4	5.3	5.2	5.0	4.5	4.1	3.5	3.1	2.5
σ_z (in Å)		0.22	0.22	0.22	0.22	0.22	0.21	0.18	0.18	0.17	0.17	0.19	0.21	0.24	0.22	0.22	0.22	0.22	0.22	0.20
σ^* (in °)		4.0	5.0	5.0	4.8	4.5	4.2	3.6	3.4	3.2	3.0	4.0	4.0	4.6	4.6	4.3	4.6	4.6	3.8	3.8
CSD size (in layers		4.5	4.8	5.2	5.5	5.5	5.5	5.5	5.0	5.0	4.5	4.5	4.2	4.7	4.7	5.0	5.1	5.0	5.0	5.0
Mixed layer 1	Ab (%)	48	49	38	39	34	33	28	28	19	21	14	28	21	17	14	10	9	7	5
	3W	3	2	2	2	2	2	2												
	2W	97	97	97	96	96	96	96	97	96	88	85	74	74	68	68	65	60	60	58
	1W		1	1	2	2	2	2	3	4	12	15	11	11	15	15	18	20	20	20
	0W												15	15	17	17	17	20	20	22
Mixed layer 2	Ab (%)	30	32	32	28	29	25	22	19	15	11	9	7	22	32	30	38	38	40	37
	3W	50	45	40	40	40	40	40	40	40	40	35								
	2W	50	55	60	60	60	60	60	60	60	60	65	10	10	8					
	1W												60	60	62	65	65	60	55	50
	0W												30	30	30	35	35	40	45	50
Mixed layer 3	Ab (%)	17	13	10	10	12	14	18	17	32	45	46	49	45	48	42	37	42	41	47
	3W	10																		
	2W	20	30	25	20	18	18	18	10	3	3	3	3	3	3	1				
	1W	70	70	75	80	82	82	82	90	97	97	97	97	97	97	98	99	96	94	80
	0W															1	1	4	6	20
Mixed layer 4	Ab (%)	5	7	20	23	25	28	32	36	35	23	30	16	12	3	15	15	12	12	11
	3W	5																		
	2W	70	72	72	70	70	65	65	55	55	45	42	25	25	25	25	25	25	25	25
	1W	25	28	28	30	30	35	35	45	45	55	58	73	73	73	73	73	73	73	73
	0W												2	2	2	2	2	2	2	2

Note: Ab.: Relative abundance; CSD: coherent scattering domain; σ_z: fluctuation of the layer-to-layer distance (in Å); σ^*: orientation parameter(in °)